DESIGN OF A ROTOR BLADE TIP FOR THE INVESTIGATION OF DYNAMIC STALL IN THE TRANSONIC WIND TUNNEL GÖTTINGEN

B. Lütke[*], J. Neumann[†], M. Schmidt[‡]
Institute of Aeroelasticity, German Aerospace Center
Bunsenstraße 10, 37073 Göttingen

ABSTRACT

The design of a pitching blade tip wind tunnel model with a double swept planform is presented. The geometry of the model and the experimental setup for the investigation of dynamic stall are shown. Steady and unsteady RANS calculations are performed to study the expected flow phenomena and identify the relevant loads at $Ma = 0.4$ and $Re = 1.2$ - $1.6 \cdot 10^6$. First unsteady dynamic stall cases reveal no significant aerodynamic pitching moments. Design features of the highly loaded carbon fiber structure are presented. Different finite element (FE) modeling approaches for the carbon composite shells bonded to a steel shaft and a spar are described in detail. Eigenfrequencies, deformation and stress distribution are evaluated. Steady coupled simulations with different spar cap orientations reveal a slightly higher negative elastic twist for forward orientated carbon fibers.

NOMENCLATURE

α, $\overline{\alpha}$	Angle of attack, mean angle of attack [°]
$\alpha_{\pm}$	Sinusoidal motion amplitude [°]
b	Airfoil model breadth (=750 mm)
$c_{(ref)}$	Airfoil (reference) chord (=160 mm)
u_∞	Free stream velocity [m/s]
r	Radial position [mm]
f	Frequency [Hz]
k	Reduced frequency: $k = 2\pi f c_{ref}/u_\infty$
C_L	Global lift coefficient
C_M	Global aerodynamic moment coefficient
L	Lift [N]
Ma	Mach number
Re	Reynolds number
T_0	Total temperature [K]
p_0	Total pressure [bar]
$\underline{u}$	Deformation vector
$\underline{f}_a$	Aerodynamic force vector
$\underline{f}_s$	Structural force vector
ω	Natural frequency
ω_k^2	kth eigenvalue
$\underline{\phi}$	Mode shape vector
$\underline{\Omega}$	Generalized stiffness matrix
Φ	Modal matrix
$\underline{q}$	Generalized coordinates
$\mathbf{M}$	Mass matrix
$\mathbf{K}$	Stiffness matrix
$\mathbf{D}$	Damping matrix
$\mathbf{H}$	Interpolation matrix

[*]benjamin.luetke@dlr.de
[†]DLR Institute of Aeroelasticity
[‡]DLR Engineering Facility Systemhaus Technik

1 INTRODUCTION

In fast forward flight or highly loaded maneuvering flight, dynamic stall leads to high negative pitching moments on the retreating blade of a helicopter. Thus, high pitch link and vibratory loads occur which can even limit the flight envelope.

The retreating blade experiences low relative flow velocities in comparison to the advancing blade, therefore high angles of attack are required to realize lateral trim. The aerodynamics of a rotor blade in its once-per-revolution (1/rev) motion has been studied by means of pitching airfoils for years ([1],[2],[3]). Although neglecting rotational effects and setting uniform inflow conditions, these investigations helped to understand dynamic stall and its dependence on Mach number, Reynolds number, mean angle of attack, pitching angle and frequency. During pitch oscillations the onset of stall is delayed to higher angles of attack than in the static case. On the upstroke, large pressure gradients lead to boundary

layer separation, vortices start to develop and travel from leading to trailing edge. High pitching moments occur when the main vortex passes of the blade. Experiments and simulations of oscillating wing tips ([4],[5]) and rotating configurations ([6],[7]) have shown similar dynamic stall phenomena as the two-dimensional cases. In addition, blade vortex interaction and the influences of the tip vortices and different planforms could be studied (see [8],[9]).

Advanced double swept helicopter rotor blade tips have the potential to extend the flight envelope through improved retreating blade stall characteristics and higher lift capabilities, respectively. Investigations have been contradicting sometimes ([8],[10]) and no single best blade tip has been emerged, yet [11]. Not only different demands but also the complexity of the flow and the large number of parameters which have to be taken into account are responsible for this uncertainty.

A double swept model rotor blade tip will be investigated on an oscillation rig in the Transonic Wind Tunnel Göttingen (TWG) in 2014/2015 to offer new insights in three-dimensional dynamic stall on a complex configuration. The patent of AIRBUS Helicopters “Noise and performance improved rotor blade for a helicopter” [12] and the airfoils EDI-M112 and EDI-M109 [3] are taken as basis for the design of the wind tunnel model. The experiment is designed to investigate the interaction of the dynamic stall vortices and the tip vortex on a double-swept rotor tip while measuring elastic deformation. The influence of reduced frequency, mean angle of attack and amplitude will be examined. A secondary focus of this experiment concerns the aeroelastic behavior of the model since the influence on the dynamic stall behavior is expected to be high. No experimental data are currently available in the public domain to describe the interaction of dynamic stall and aeroelastic deformation on a pitching blade tip. Aeroacoustical investigations are not within the scope of the present work.

In this paper the aerodynamic and structural design process of a pitching, one-sided clamped wind tunnel model (Figure 1 and 2) are presented. The wind tunnel facility and the chosen geometry are described in detail. Important structural design features and the finite element modeling of the carbon fiber model including results of modal and static analysis are shown. Steady, unsteady and coupled computational fluid dynamic (CFD) simulations are studied. Flow phenomena and integral loads of several load cases are compared.

2 EXPERIMENTAL SETUP - BLADE TIP GEOMETRY

The TWG has a cross section of 1 m x 1 m. The lower and upper wall can be adapted. Optical windows in the wind tunnel sidewalls and in the hydraulic test oscillation rig [13] offer access for optical systems. Flow phenomena will be resolved by 60 unsteady pressure transducers (see Figure 1), pressure sensitive paint and a piezo balance [14]. Aeroelastic measurements will be performed by 6 acceleration sensors and a 3D-marker-tracking system to record deformation. Further aerodynamic and thermodynamic data concerning the experimental setup are listed in Table 1.

Table 1: Geometric and aerodynamic boundary conditions

p_0 (min.-max.)	0.3 - 1.5 bar
T_0 (min.-max.)	293 - 315 K
Ma (min.-max.)	0.3 - 0.9
Re_{max} at $Ma = 0.4$	$2 \cdot 10^6$
Reference Chord c	0.16 m
Wind tunnel cross section	1 m x 1 m
f_{max} at $\alpha = \pm 1$	80 Hz
$\alpha_{\pm,max}$ at $f = 6.6$ Hz	8°
k at $Ma = 0.4$ and $f = 6.6$ Hz	0.05

A maximal model span of $b = 750$ mm is chosen in order to limit the wind tunnel wall interference on the blade tip. A high aspect ratio of 4.7 is chosen because of a real rotor blades first onset of separation which appears at a radial position of approximately 70-90%.

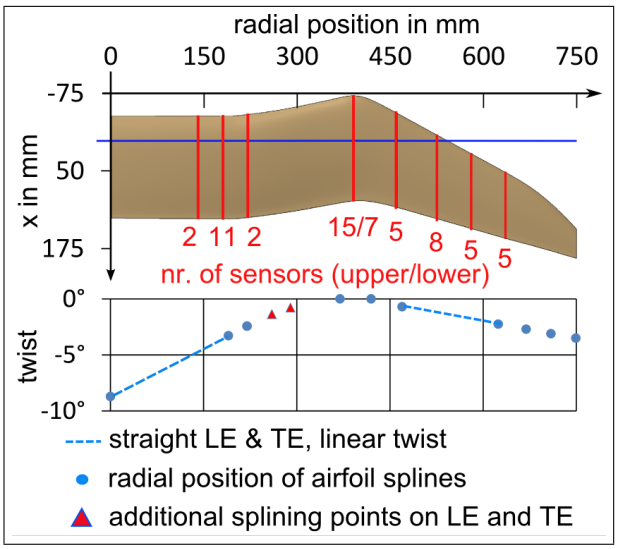

Figure 1: Planform of wind tunnel model; location of pressure transducers (top); spanwise twist and spline locations (bottom)

The planform shown in Figure 1 is derived from the parameterized patent of AIRBUS-Helicopters [12]: a rectangular section at the root, a forward swept section, a tapered backward swept section and a parabolic shape for the outside section. The backward sweep is used to relieve the effects of compressibility at the advancing blade in forward flight. The forward sweep helps to move the center of gravity forward and keeps the aerodynamic centre near the quarter-chord feathering axis of the blade. Thus, pitch link loads and vibrations can be

reduced [11]. The pitch axis is positioned at the quarter-chord of the root section. The axis is flush with the wind tunnel wall, a distance of 1.5 mm between wind tunnel wall and root airfoil ensures contactless operation.

The EDI-M112 airfoil with 12% thickness is used for the inner unswept part since it shows soft trailing edge stall at low Mach number ($Ma = 0.3$ - 0.4) [3]. The EDI-M109 airfoil with 9% thickness is used for the forward/backward swept part where higher Mach numbers occur. Along with the tapered outer part a low drag coefficient is expected.

The twist angle of helicopter rotor blades usually declines gradually from the root to the tip. In case of the pitching wind tunnel model the twist is decreased at the root in order to avoid dynamic stall being triggered by the separation at the wind tunnel wall. Thus, the position of inner dynamic stall moves to a radial position of $r \approx 250$ mm, where forward sweep begins. Here the sectional lift is at its maximum while the interference of the wind tunnel wall is negligible. The blade tip model has no anhedral to reduce measurement complexity. The chord is nearly constant, $c = 165$ mm (small variations at the notch), until $r = 400$ mm. At the tip the chord is $c = 100$ mm. The trailing edge is slightly modified at the tapered part to maintain a thickness of at least $t_{TE} = 0.5$ mm. The small chord length and the thin airfoils limit considerably the mounting space for pressure transducers and acceleration sensors.

CATIA V5 software is used to generate the geometry. Ten airfoil splines, see Figure (1), with more than 250 points each are the basis for defining the surface spline. The leading edge curve and the upper and lower trailing edge curves are used as guide curves for the surface spline. They are generated by straight lines in the linear parts and splines through several additional points in the curved parts of the blade tip. Using more airfoil splines for the generation of the surface spline leads to oscillations in the spline surface.

3 CARBON COMPOSITE MODEL - FINITE ELEMENT MODELING

The pitching wind tunnel model is designed as a carbon fiber model because high bending and torsional stiffness, low weight and sufficient mounting space for instrumentation are required. A high mass inertia in torsion and a strong bending-torsion coupling due to the planform is expected [15]. In order to limit positive elastic twist a specific bending-torsion coupling is a further design goal. Since no centrifugal stiffening effects as under real flight conditions occur in the experiment, a high bending stiffness is a secondary design goal.
Thus, the wind tunnel model is built as an upper and a lower carbon composite shell (Table 2) which are bonded to a steel shaft and a spar (Figure 2). At the leading edge the upper and lower shell are connected by a leading edge bonding.

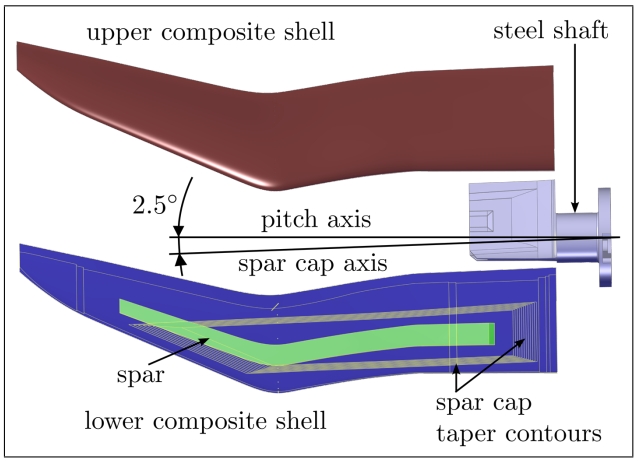

Figure 2: Catia V5 model of the rotor blade tip

Table 2: Laminate with M46J plies and integrated spar cap of 1 mm thickness; first ply on outer contour

Number	Thickness in mm	Orientation in °
1	0.115	-45
2	0.115	45
3	0.115	90
4	0.115	0
5	0.115	23
6	0.115	-23
7-18	1.38	-2.5
19	0.115	-23
20	0.115	23
21	0.115	0
22	0.115	90
23	0.115	45
24	0.115	-45

The upper and lower shell are built using the unidirectional lamina M46J. A fiber volume fraction of $\rho_f \approx 50\%$ can be obtained by the hand lay-up method. Integrated unidirectional spar caps run from the steel shaft in spanwise direction, tapering out at the beginning of the backward sweep (Figure 2). Their fibers, which carry the main bending loads, are orientated forward at an angle of $2.5°$ in order to follow the spar contour and enforce the bending-torsion coupling. The overlap of the unidirectional layers on the steel shaft is tapered 26:1 in spanwise direction and 8:1 in chord direction in order to reduce stress concentrations [16]. The spar consists of a ROHACELL core covered with $\pm 45°$ laminate M40J. It experiences shear forces as a result of the lift and torsional loads as a result from the aerodynamic moments and forced pitching inertial moments. The leading edge bonding is a support structure of 0.8 mm thick laminate M40J ($\pm 45°$). Bonded to the composite shells and to the spar, a steel shaft (Figure 3) transfers the loads to the Piezo balance which is interconnected between the model shaft and the hyraulic oscillation rig.

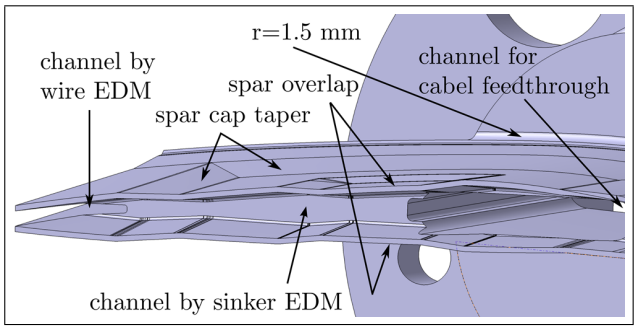

Figure 3: 42CrMo4 steel shaft with tapered channels for homogeneous stress distribution

The distance between the wind tunnel wall and the root airfoil is 1.5 mm. To avoid high stress concentrations the steel shaft has a corner radius of $r = 1.5$ mm. A tapered channel is manufactured using sinker electrical discharge machining (EDM) at the spanwise end of the steel shaft. Thus, a more homogeneous stress distribution in the laminate and the steel is obtained. Another tapered channel is manufactured using wire-cut EDM at the chordwise end of the steel shaft for the same reason. Two overlapping regions between steel shaft and spar allow torsional load transfer between spar and root. A tapering of about 12:1 in spanwise and chord direction is provided for the overlapping weave of the spar. The shaft is hollow in order to integrate the cables and pressure reference tubes of the unsteady pressure tabs and the cables of the acceleration sensors. After the instrumentation of both shells they are bonded together.

Three ANSYS^{TM} [17] finite element model versions (see Table 3) have been established using shell elements for the laminate and volume elements for the spar, bonding and shaft. The applied shell element SHELL281 is described by the first-order shear-deformation theory (Mindlin-Reissner). It has eight nodes with three translational and three rotational degress of freedom at each node. The applied solid element SOLID186 is defined by 20 nodes having three translational degrees of freedom at each node. All material properties and deformations are considered linear. The shell elements are placed on the outer contour of the model because their thickness is not known in advance. Since the contour of the steel shaft depends on the final thickness of the laminate, an estimation of this thickness is required at the beginning. Based on existing models, laminate thicknesses of $t = 1.8$ mm in the unreinforced region and $t = 3.0$ mm in the region of the integrated spar caps are chosen. Thus, the 2D-shell elements of the outer composite surface and the 3D-volume elements of the steel shaft have to be connected over a distance of the presumed thickness of the laminate. The same holds for the connection outer surface and the ROHACELL core of the spar as well as for the connection outer surface and leading edge bonding.

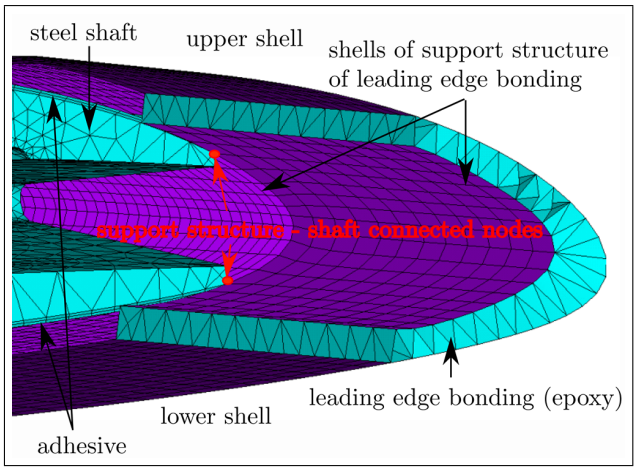

Figure 4: FE modeling of the leading edge bonding (rigid links between shaft adhesive and outer contour are not displayed)

For all model versions, the support structure of the leading edge bonding is connected to the outer contour by volume elements with epoxy properties (Figure4). In order to reduce modeling complexity, the leading edge bonding is directly connected to the shaft and widens abruptly at the end of the shaft. In reality, a tapered widening is used and a small gap is located between support structure and shaft. The adhesive of the leading edge bonding is about ten times thinner in reality than in the model.

Two modeling approaches for the connection of outer surface - shaft and outer surface - spar are proposed in the following (see Table 3). In the first model 'V1$_{GUD2.5}$', which is shown in Figure (5), the gap is filled with 3D-volume elements with the material properties of epoxy.

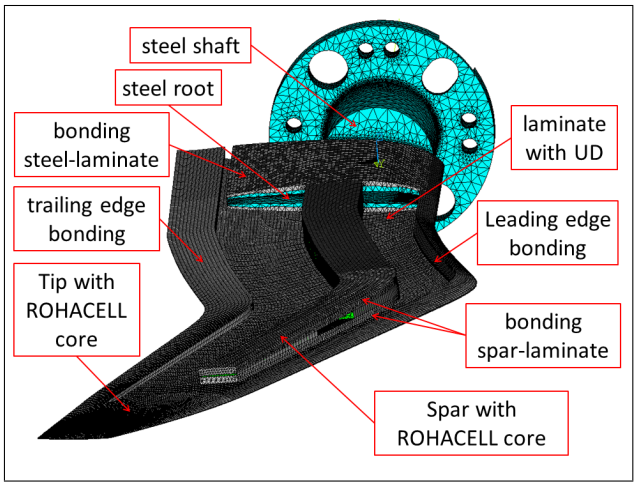

Figure 5: FE modeling approach 'V1$_{GUD2.5}$' with overrated bonding thickness for simple shell-solid connection

This kind of modeling leads to an adhesion thickness up to 10 times thicker than in reality.

Table 3: Modeling approaches and model versions

-	Approach 1	Approach 2	
-	V1$_{GUD2.5}$	V2$_{CUD2.5}$	V3$_{CUD0}$
Spar cap orient. in °	2.5	2.5	0.0
Adhesive	too thick	realistic	realistic
Connection 2D-3D-Elem.	3D-solids (epoxy)	CERIGs rigid links	CERIGs rigid links
Mass in kg	6.95	7.19	7.19
Nr. of shells	65k	97k	97k
Nr. of shells	638k	1084k	1084k

In the second, more sophisticated modeling approach (model versions 'V2$_{CUD2.5}$' and 'V3$_{CUD0}$') an epoxy volume of $t = 0.3$ mm thickness is implemented on the shaft (Figure 4) and connected by rigid links (CERIG) with the 2D-shell elements on the outer surface.
The core of the ROHACELL spar is modeled with 3D-volume elements. The outer faces are covered with 2D-shell elements simulating the $\pm 45°$ weave. In version 'V1$_{GUD2.5}$' these elements are connected to the 2D-shell elements on the outer surface by 3D-volume elements with epoxy properties. In 'V2$_{CUD2.5}$' and 'V3$_{CUD0}$' a realistic 0.3 mm thin epoxy volume is modeled parallel to the upper and lower surface of the core (Figure 6).

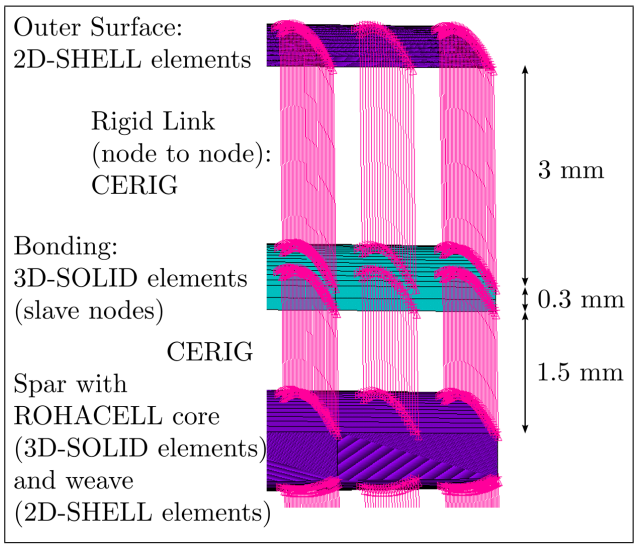

Figure 6: FE modeling approach 'V2$_{CUD2.5}$' and 'V3$_{CUD0}$' with realistic adhesive thickness and rigid links

The upper and lower surface of the spar are connected by rigid links with the epoxy volumes. The distance of 1.5 mm is a first approximation of the weave thickness which covers the core. The outer surface of the thin epoxy volume is connected by rigid links to the 2D-shell elements on the outer contour. This is only possible if the connected surfaces have the same node distribution. Two models with different laminate layouts are presented for the second modeling approach. The first model 'V2$_{CUD2.5}$' has the same laminate layout as 'V1$_{GUD2.5}$', listed in Table 2. In the second model 'V3$_{CUD0}$', the unidirectional fibers of the spar cab are orientated in the direction of the pitching axis and not in 2.5-degree direction (Figure 2).The support of the axis is modeled with BEAM188 elements for all modeling approaches and all models. Constraints in x-, y- and z-direction are applied to the bearing positions of the hydraulic oscillation rig (Figure 8).

A typical undamped modal analysis is performed. The classical eigenvalue problem

$$\mathbf{K}\underline{\phi}_i = \omega_i^2 \mathbf{M}\underline{\phi}_i \tag{1}$$

is solved using the Block Lanczos method. The first ten eigenfrequencies of the three finite element models are listed in Table 4.

Table 4: Eigenfrequencies of the 3 different FE-models; B=Bending, T=Torsion, L=Lag

Mode Nr.	Shape	Frequency [Hz]		
		V1$_{GUD2.5}$	V2$_{CUD2.5}$	V3$_{CUD0}$
1	1st B	60.3	64.4	64.9
2	1st B-L	158.1	171.0	171.3
3	2nd B-L	176.0	190.7	190.9
4	2nd B	324.8	341.2	339.4
5	1st T	406.4	410.5	409.4
6	3rd B	471.2	498.4	499.1
7	B-L-T	594.8	619.9	620.6
8	2nd T	696.4	706.4	704.5
9	B-L	793.4	829.7	832.7
10	3rd T	898.48	913.8	915.1

The first modeling approach 'V1$_{GUD2.5}$' has lower eigenfrequencies than the model versions V2$_{CUD2.5}$ and V3$_{CUD0}$ because of its higher mass (Table 3). The corresponding moments of inertia for 'V1$_{GUD2.5}$' and V2$_{CUD2.5}$ are listed in Table (5).

Table 5: Moments of inertia in Nm^2, CS from Figure 1; 'V1$_{GUD2.5}$' (top), 'V2$_{CUD2.5}$' (bottom)

$$\begin{pmatrix} Ixx & Ixy & Ixz \\ Ixy & Iyy & Iyz \\ Ixz & Iyz & Izz \end{pmatrix} = \begin{pmatrix} 0.326 & -0.015 & -0.001 \\ -0.015 & 0.011 & 0.001 \\ 0.001 & 0.001 & 0.331 \end{pmatrix}$$

$$\begin{pmatrix} Ixx & Ixy & Ixz \\ Ixy & Iyy & Iyz \\ Ixz & Iyz & Izz \end{pmatrix} = \begin{pmatrix} 0.303 & -0.013 & -0.001 \\ -0.013 & 0.011 & 0.001 \\ 0.001 & 0.001 & 0.307 \end{pmatrix}$$

The modeshapes look very similar for all three cases. The corresponding modeshapes of version 'V3$_{CUD0}$' are shown in Figure 7.

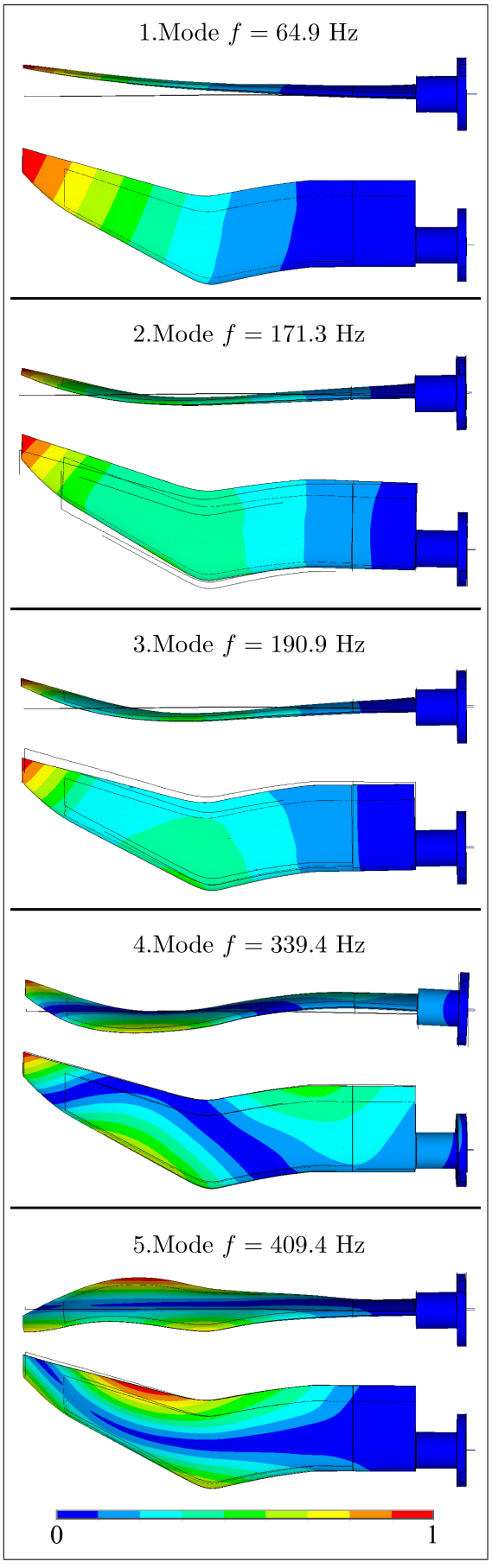

Figure 7: Modeshapes of V3$_{CUD0}$

The stress analysis procedure is presented for load case LC3 (Table 6) in the following. The aerodynamic forces are selected from the CFD-simulation at the angle of attack where the highest forces $F_Z = 1320$ N occur (Figure 16). The loads acting on the CFD-nodes f_a are interpolated on the FE-nodes f_s.

$$f_s = \mathbf{H}^T f_a \tag{2}$$

The transposed coupling matrix $\mathbf{H}^T$ is generated by using a radial basis function approach, presented in [18]. A static analysis is performed with the interpolated loads in ANSYS. The deformation of V2$_{CUD2.5}$ is shown in Figure (8).

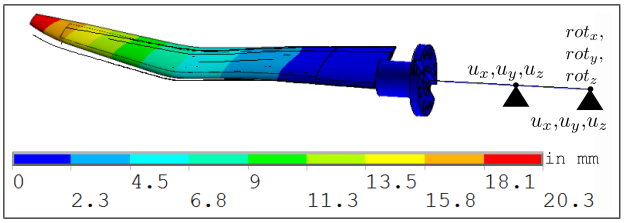

Figure 8: Elastic deformation of LC3 for static applied loads; $F_Z = 1320N$

The same loads applied to 'V1$_{GUD2.5}$' lead to a very similar bending deformation with a 0.2 mm higher maximal deformation at the tip.

In the next step, the forced pitching motion is simulated by means of a harmonic analysis. Therefore, the aerodynamic forces are deleted and the y-rotation constraint is adapted. The equation of motion is divided for the unknown displacements $\underline{u}_a$ and for the prescribed displacements $\underline{u}_b$.

$$\begin{bmatrix} \mathbf{M}_{aa} & \mathbf{M}_{ab} \\ \mathbf{M}_{ba} & \mathbf{M}_{bb} \end{bmatrix} \begin{bmatrix} \underline{\ddot{u}}_a \\ \underline{\ddot{u}}_b \end{bmatrix} + \begin{bmatrix} \mathbf{D}_{aa} & \mathbf{D}_{ab} \\ \mathbf{D}_{ba} & \mathbf{D}_{bb} \end{bmatrix} \begin{bmatrix} \underline{\dot{u}}_a \\ \underline{\dot{u}}_b \end{bmatrix} + \begin{bmatrix} \mathbf{K}_{aa} & \mathbf{K}_{ab} \\ \mathbf{K}_{ba} & \mathbf{K}_{bb} \end{bmatrix} \begin{bmatrix} \underline{u}_a \\ \underline{u}_b \end{bmatrix} = \underline{0}. \tag{3}$$

A constant modal damping of $\xi = 0.02$ is defined. With the harmonic approach

$$\underline{u} = \underline{\hat{u}} \cdot e^{j\omega t} \tag{4}$$

the equations can be rewritten as

$$\left(-\omega^2 \mathbf{M}_{aa} + j\omega \mathbf{D}_{aa} + \mathbf{K}_{aa}\right) \underline{\hat{u}}_a = \left(\omega^2 \mathbf{M}_{ab} - j\omega \mathbf{D}_{ab} - \mathbf{K}_{ab}\right) \underline{\hat{u}}_b \tag{5}$$

and

$$\left(-\omega^2 \mathbf{M}_{ba} + j\omega \mathbf{D}_{ba} + \mathbf{K}_{ba}\right) \underline{\hat{u}}_a = \left(\omega^2 \mathbf{M}_{bb} - j\omega \mathbf{D}_{bb} - \mathbf{K}_{bb}\right) \underline{\hat{u}}_b. \tag{6}$$

As one can see from the equations above, the result $\underline{\hat{u}}_a$ is generally complex

$$\underline{\hat{u}}_a = \underline{\hat{u}}_{a,Re} + j \cdot \underline{\hat{u}}_{a,Im}. \tag{7}$$

Inserting equation (7) into equation (4) and extracting the physically relevant real part leads to

$$(8)\quad \underline{u}_a(t) = \Re(\underline{\hat{u}}_a e^{j\omega t}) = \underline{\hat{u}}_{a,Re}\cdot\cos(\omega t) - j\cdot\underline{\hat{u}}_{a,Im}\cdot\sin(\omega t)$$

The deformation in z-direction of the real part $\underline{\hat{u}}_{a,Re}$ and the deformation of the imaginary part $\underline{\hat{u}}_{a,Im}$ of equation (8) are shown in Figure (9).

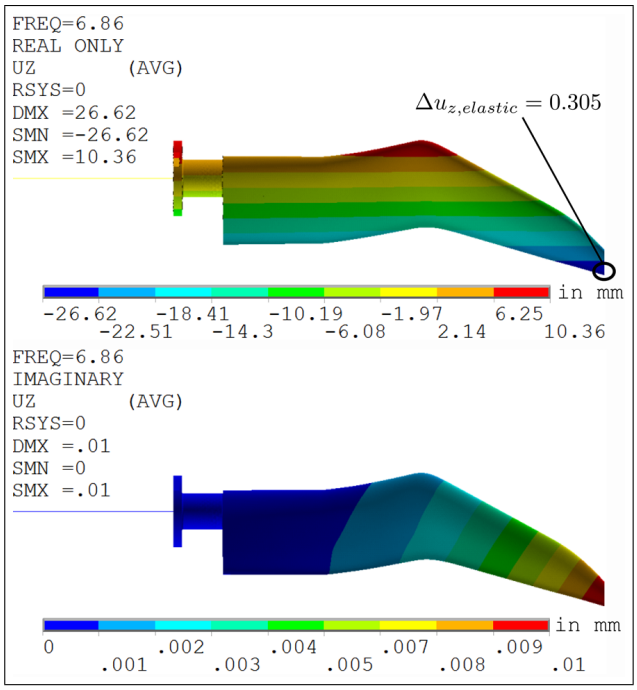

Figure 9: Deformation for harmonic motion ($f = 6.86$ Hz and $\alpha_{\pm} = 8°$); real part (top), imaginary part (bottom)

Thanks to lightweight construction and the short chord length of the model, the moments of inertia are small which leads to very small deformations due to harmonic motion. The real part shows the blade tip at time $t = 0$, where the rotational acceleration is at its maximum. The elastic deformation is obtained by subtracting the rigid motion from the overall deformation. The maximal elastic deformation $u_z = 0.305$ mm at the trailing edge of the outer tip is very small compared to the deformation due to the static applied loads.
The imaginary part shows the blade tip at time $t = T/4$. The small elastic deformation in z-direction $u_z = 0.01$ mm shows that the phase difference for the applied load case is very small. Thus, the real part is superpositioned on the static solution. In case of higher pitching frequencies or higher amplitudes, the phase shift has to be taken into account and reveal the point of highest deformation or stresses, respectively.

Stresses in laminate, bonding and shaft are presented for the superpositioned load case in the following.

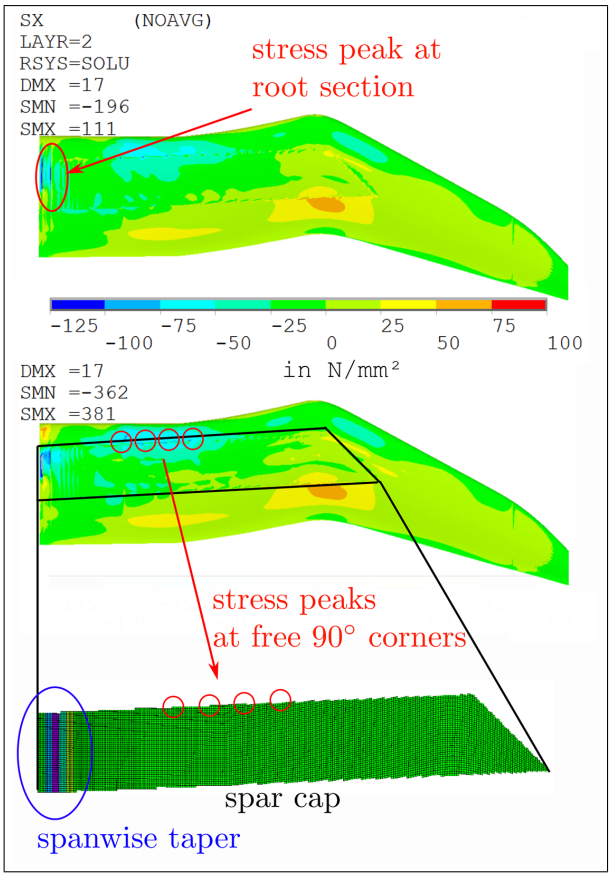

Figure 10: Stress σ_x in fiber direction of $+45°$ layer; $V1_{GUD2.5}$ (top), $V2_{CUD2.5}$ (bottom)

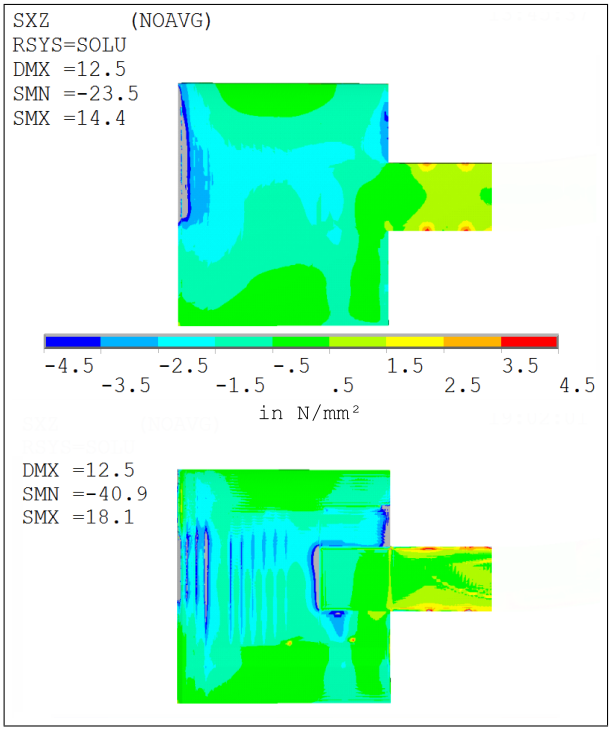

Figure 11: Shear stress τ_{xz} in bonding on upper shaft and spar; $V1_{GUD2.5}$ (top), $V2_{CUD2.5}$ (bottom)

The highest stress peaks occur in ply 23 (+45° orientation, see Table 2) at the free corners of the spar cap reinforced shells (Figure 10). The effect is enforced by the neglected chordwise tapering in the FE model. The stresses in all layers show peaks at the root section since the material thickening of the shaft leads to a strong change in stiffness. Spanwise tapering at the root section in order to prevent edge delaminations is included in the FE model. The resulting spanwise shear stress distributions τ_{xz} of the bonding are shown in Figure 11. The differences of the two modeling approaches are more obvious but similar to the stress distribution of the plies. The peaks and the overall shear stresses of $V2_{CUD2.5}$ are significantly higher than in $V1_{GUD2.5}$. The thicker adhesive exhibits lower stresses at the same deformation. The bonding shear stresses of $V2_{CUD2.5}$ have a more homogeneous distribution. In order to reduce the stress peaks in the adhesive at the spanwise end of the shaft a more sophisticated channel is cut in the final shaft (compare Figure 3 and 11). The constant material thickness of 0.8 mm is introduced at the end of the shaft. Thus, a more homogeneous stress distribution in the adhesive is expected. The tapering of the spar overlap is not included in the finite element model. Therefore, singularities occur at the edges of the overlap. Further stress peaks occur at the position of holes in the spar. In the final wind tunnel model these holes for cable feedthrough have been moved in spanwise direction where cut loads are smaller. Considering the maximal allowed bonding shear stress of 7 [MPa] for linear material behavior, the safety margin is greater than 1.5. The stresses occuring in the bonding are the bottle neck of the structural design and limit the possible load cases. A bending moment peak of $M_x = 450$ Nm and a global lift of $L = 1400$ N should not be exceeded.
In the steel shaft the highest von-Mises stresses occur at the root section (Figure 12).

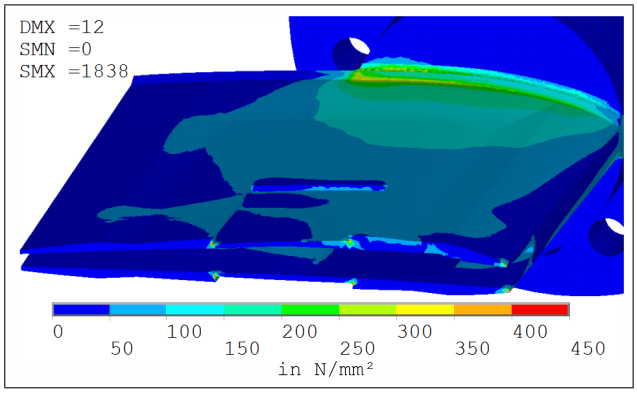

Figure 12: Von Mises stress in shaft ($V2_{CUD2.5}$)

Singularities can be found at the spar - shaft connection and at the leading edge bonding - shaft connection.

The final strength analysis which is not reproduced in this paper, is performed using the Hashin criteria [19].

4 CFD-SIMULATIONS

Three types of computational fluid dynamic (CFD) simulations with various degrees of complexity are used to generate load cases (LC) and study the occurring flow phenomena: steady (s), unsteady (u) and unsteady cases with grid deformation (u-gd), see Table 6.

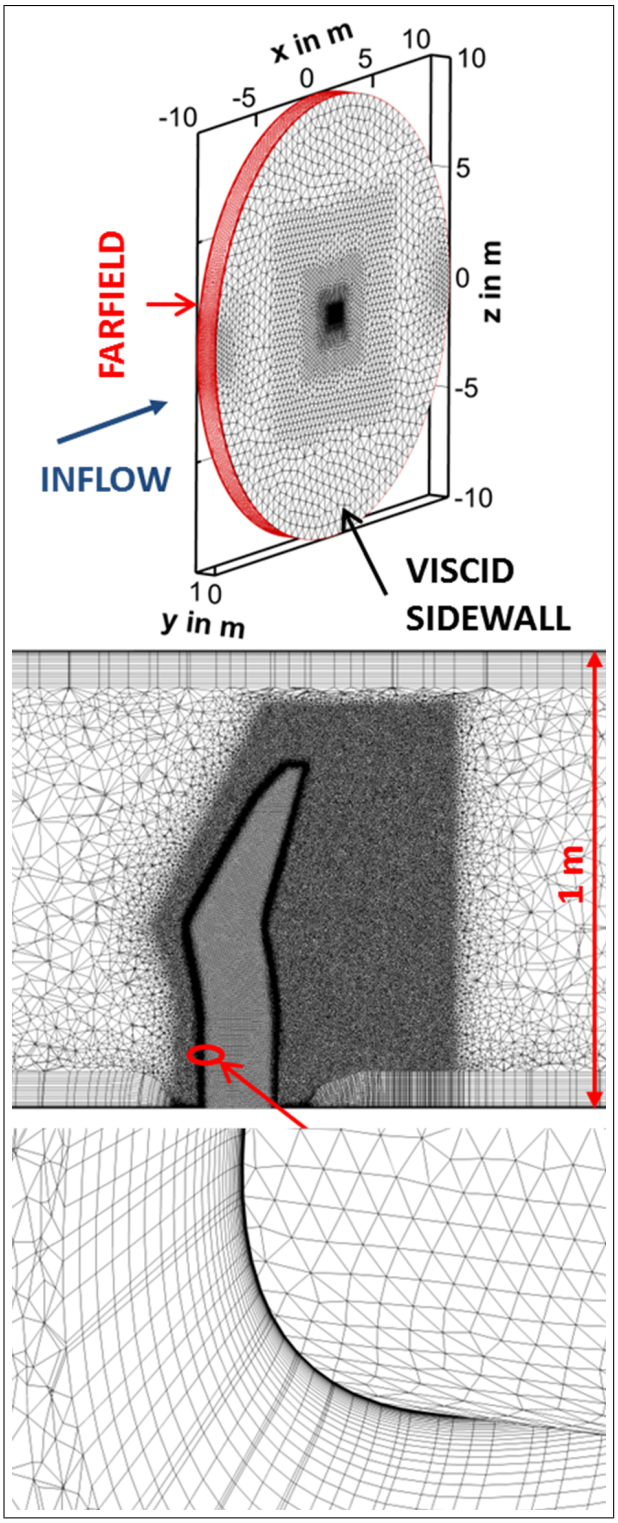

Figure 13: CFD-grid Version 5; Geometric properties

The numerical CFD simulations are performed by the node-based finite-volume solver DLR-TAU [20]. The inviscid fluxes are discretized using a second order central scheme. All simulations are fully turbulent, a two-equation Menter SST turbulence model [21] is applied. The numerical grids are created by the unstructured grid generator CENTAUR^{TM}. The same geometric properties and boundary conditions are used for all CFD-grids, see Figure 13.

Table 6: Aerodynamic load cases at $Ma = 0.4$; max. forces and moments calculated on grid V4

load-case	type	Re	α in $\circ$	k	$F_{Z,(max)}$ in N
LC1	s	$1.6 \cdot 10^6$	10	-	1146
LC2	s	$1.2 \cdot 10^6$	15	-	1135
LC3	u	$1.6 \cdot 10^6$	10 ± 8	0.05	1766
LC4	u	$1.2 \cdot 10^6$	10 ± 8	0.05	1322
LC5	u-gd	$1.2 \cdot 10^6$	10 ± 8	0.05	1310

Viscous sidewalls with 1 m distance and a farfield with radius $r = 10$ m (60 times the chordlength) are implemented. By accepting this rather short farfield radius, the growth of the boundary layer on the viscous sidewalls corresponds well with the inflow conditions of the TWG [22]. Preliminary simulations with symmetry boundary conditions on the sidewalls are not presented since no conclusions can be drawn with respect to the separation behavior at the wind tunnel wall. The root airfoil section is directly connected to the viscous wall and the gap of 1.5 mm is not taken into account.

In the first step steady RANS simulations are carried out. A mesh convergence study is performed for LC1 (see Table 6). The global results and the grid properties are shown in Table 7.

Table 7: LC 1 simulated with different Grids

	V1	V2	V3	V4
Nr. of Points ($\cdot 10^6$)	9.0	5.7	11.1	8.3
Nr. of Surf. P.	170k	109k	182k	127k
Nr. of Surf. TE P.	15.6k	2.1k	16.3k	5.4k
Nr. of B.-Lay.	30	40	40	40
max. y^+	1.49	1.35	1.85	1.42
C_L	0.837	0.849	0.850	0.849
C_D	0.038	0.036	0.036	0.036
C_{My}	-0.065	-0.068	-0.069	-0.068

The global values C_L, C_M and C_D are very similar, even between the Version 2 with 5.7 million points and Version 3 with 11.1 million dofs. Since the flow of this loadcase is attached, one might argue that a grid convergence study for unsteady cases with high angles of attack is appropriate. This investigation is beyond the scope of the work. The numerical grid V4, presented in Figure 13, was used for all final steady, unsteady and coupled simulations since it has shown the most stable performance for the unsteady cases. The surface resolution is higher than for grid V2 and surface nodes are more physical distributed than in grid V1. Grid V3 was neglected because of its huge size. The value of $y^+ > 1$ occurs only in very small regions of the domain. Furthermore, the Reynolds number was decreased to $Re = 1.2 \cdot 10^6$ in the structural design process which consequently leads to lower values of y^+.

A first impression of the aerodynamic flow field and the surface forces at high angles of attack can be deduced from the steady load case LC2.

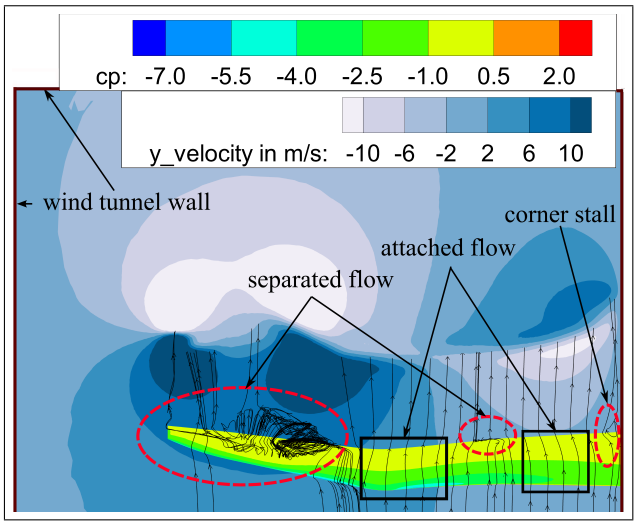

Figure 14: LC2 with grid V4; $Ma = 0.4$, $Re = 1.2 \cdot 10^6$, $\alpha = 15^\circ$

The velocities in y-direction are shown on a plane about 200 mm downstream from the blade tip. The velocities are below 2 m/s on the left viscous wall which shows that the interaction of tip vortex and left wind tunnel wall is small. Three regions of separation can be seen on the upper blade tip surface. Hereby, we deduce that the modification of the twist at the root is sufficient to separate wind tunnel wall separation and first inboard separation on the model. This is confirmed by the unsteady results presented in the following.

In the second step, unsteady RANS simulations with a rotating grid are performed. This simulation configuration leads to fast converging results, starting with a converged steady solution. At 2000 physical time steps per period and 100-1000 inner iterations, depending on a Cauchy Convergence criterion, more than two periods are only calculated for LC3 with grid V1 in order to check periodicity. The second period is already in good agreement with the third period, see Figure 15.

In order to check the influence of different grids, this load case is also simulated with grid V3 and V4 where the physical distribution of nodes is improved. They show better agreement in the C_L peaks. However, the reattachment region differs significantly and a second lift peak is only resolved by grid V3 which is probably less dissipative.

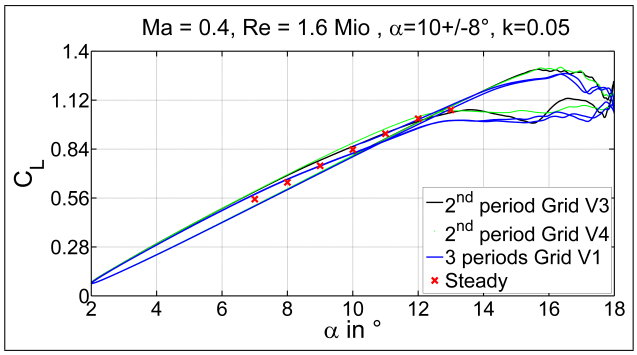

Figure 15: LC3: $Ma = 0.4$, $Re = 1.6 \cdot 10^6$; $C_L - \alpha$ distribution for different grids

For all further simulations grid V4 is used. Comparing the $C_L - \alpha$ distribution at $Re = 1.6 \cdot 10^6$ to the $C_L - \alpha$ distribution at $Re = 1.2 \cdot 10^6$ in Figure 16 no significant differences can be seen.

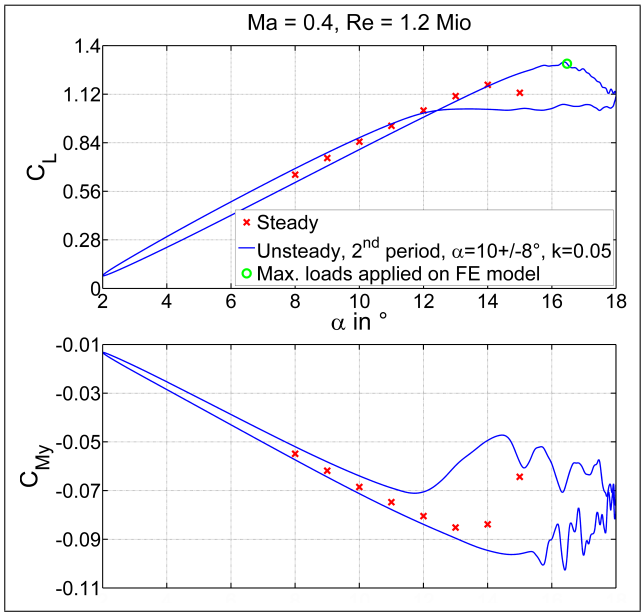

Figure 16: LC4: $Ma = 0.4$, $Re = 1.2 \cdot 10^6$; $C_L - \alpha$ distribution (top), $C_{My} - \alpha$ distribution (bottom)

The delayed and increased lift peak in comparison to the steady case is clearly visible for both Reynolds numbers. There is no significant global pitching moment peak in the $C_{My} - \alpha$ distribution as presented for the two dimensional cases in [3].

In Figure 17 the flowfield at $\alpha_{inst} = 16.08^\circ \nearrow$ (in upstroke) is shown. The flow phenomena are similar to the flow phenomena of the presented steady case, shown in Figure 14. The tip vortex merges with the dynamic stall vortex of the backward swept part. A smaller inboard separation occurs at $r \approx 250$ at the trailing edge. Inner and outer vortices pass the trailing edge at different angles of attack. Therefore, no single pitching moment peak appears in Figure 16. There are two regions of attached flow: one at the notch and one between the corner stall at the root and the desired separation region at r ≈ 250 mm. The rotating viscous sidewalls of this configuration do not match the non-rotating wind tunnel walls since they transport fluid. The development of shear layers near the walls can be deduced from the increasing vorticity shown in Figure 17.

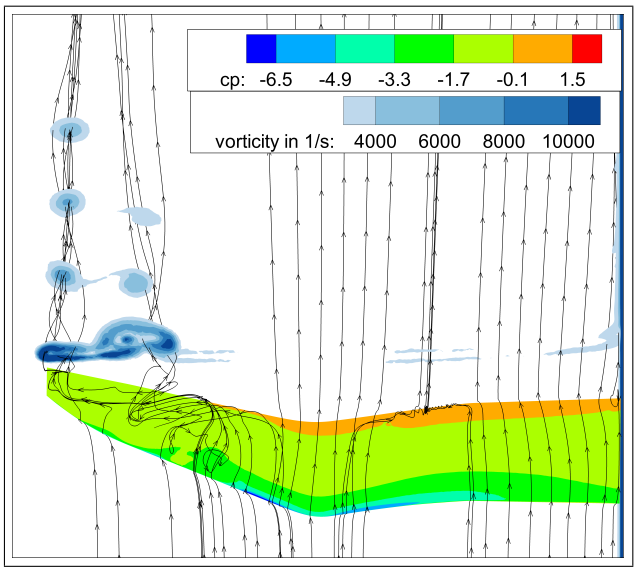

Figure 17: LC3: $Ma = 0.4$, $Re = 1.6 \cdot 10^6$ at $\alpha_{inst} = 16.08^\circ \nearrow$; Upstroke with rotating grid

In the third step unsteady RANS simulation with grid deformation are carried using the DLR-TAU deformation tool which is based on radial basis functions [23]. All surface points of the aerodynamic mesh of the blade tip are moved in a rigid body motion. The difference between non-rotating sidewalls to the former approach is investigated. The instantaneous flowfields at $\alpha_{inst} = 16.08^\circ \nearrow$ of loadcase 4 are compared in Figure 18.

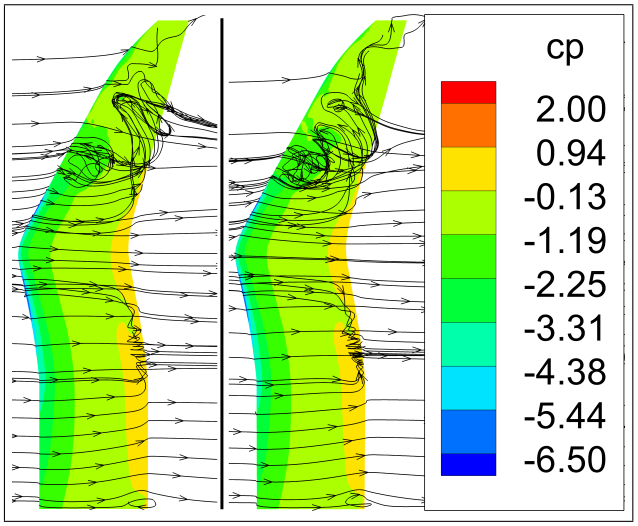

Figure 18: LC4: $Ma = 0.4$, $Re = 1.2 \cdot 10^6$ at $\alpha_{inst} = 16.08^\circ \nearrow$; Grid deformation (left) vs. rotating grid (right)

The differences in the pressure distribution c_p and in the streamlines are so small that the simulation configuration with the rotating grid seems accurate enough to investigate even the main flow phenomena of the pitching blade tip. Comparing the F_Z-peak of one period, the difference is $\Delta F_{Z,peak} = 12N$ which is negligible for structural design criteria. The regions of separation and the structure of the vortices are the same as at $Re = 1.6 \cdot 10^6$ shown in Figure 17.

5 CFD-CSD COUPLED SIMULATIONS

For all steady fluid-structure interaction simulations the in-house coupling software PyCSM has been used. In the implemented weak coupling method the flow solver and the structural solver operate separately. PyCSM uses a modal approach with the generalized coordinates $\underline{q}$, the structural forces $\underline{f}_s$ and the structural modal matrix $\bar{\Phi}_s$. The transposed coupling matrix from Equation 3 is introduced into the general equation of motion written in generalized coordinates.

$$\Omega \cdot \underline{q}(t) = \Phi_s^T \mathbf{H}^T \underline{f}_a(t) \tag{9}$$

The interpolation procedure between structural and aerodynamic modeshapes

$$\Phi_a = \mathbf{H}^T \Phi_s \tag{10}$$

is performed only once as a pre-processing step. In order to reduce the calculation effort the set of structural interpolation points is reduced (see Figure 19).

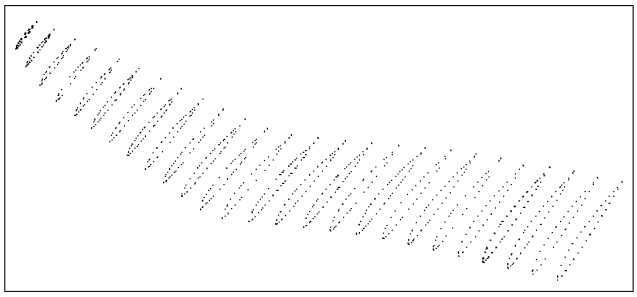

Figure 19: Structural coupling points

The model is divided in 15 spanwise coupling regions where the splining procedure is carried out. The fluid-structure coupling procedure is presented in [24]. The aeroelastic simulations for load case 6 (Table 8) are started with a converged simulation of the rigid blade tip. Using 30 modehapes the deflection at the blade tip is converged ($u_n - u_{n-1} < 0.1$ mm) after three iterations.

Table 8: Load case 6 for steady coupled simulations

	Ma	Re in Mio.	α
LC6	0.4	1.2	10

The bending deformation of the quarter chord line and the elastic twist of all FE model versions (Table 3) are shown in Figure 20.

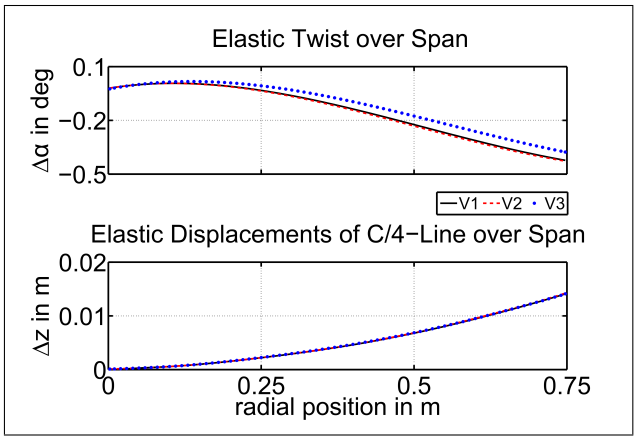

Figure 20: Elastic twist (top); bending (bottom)

The bending deformation of all three FE models is nearly the same. The deformations $u_{z,TE-TIP}$ on the trailing edge of the tip are listed in Table 9.

Table 9: Results of all FE model versions for LC6

FE model	Type	$u_{z,TE-TIP}$	C_L
V1$_{GUD2.5}$	coupled	14.34 mm	0.838
V2$_{CUD2.5}$	coupled	14.46 mm	0.838
V2$_{CUD2.5}$	rigid-static	14.87 mm	0.846
V3$_{CUD0}$	coupled	14.30 mm	0.841

Due to the different carbon fiber orientation of the spar cab the negative elastic twist of V3$_{CUD0}$ is lower than in V1$_{GUD2.5}$ and V2$_{CUD2.5}$. Consequently the global lift coefficient is increased by 0.03 in V3$_{CUD0}$. Still, the difference is small. The effect of the stronger bending torsion coupling (V1$_{GUD2.5}$ and V2$_{CUD2.5}$) will be increased for higher load cases or a higher angle ($\alpha > 2.5°$) of the forward orientated spar cabs. The good agreement between V1$_{GUD2.5}$ and V2$_{CUD2.5}$ shows that the overall stiffness is not influenced significantly by the different modeling approaches of the bonding.

A static FE analysis with the CFD-loads of a rigid simulation is compared to the coupled simulation. The deformation u_Z of the trailing edge point at the tip of V2$_{CUD2.5}$ is 0.41 mm higher for the rigid-static case (see Table 9). The reason are the higher aerodynamic loads from the CFD-simulation with the rigid model. No negative elastic twist, as seen in the coupled simulations, reduces the aerodynamic forces.

6 CONCLUSIONS

The aerodynamic and structural design of a pitching double swept rotor blade tip for the investigation of three-dimensional dynamic stall in the TWG Göttingen is pre-

sented. A high aspect ratio of 4.7 leads to a very limited instrumentation space and highly loaded carbon composite shells. The shear stresses τ_{xz} occuring in the bonding between steel shaft and carbon composite shells limit the possible load cases. Two different modeling approaches for the bonding are proposed. Both show a very similiar global deformation behavior for steady applied loads and for steady state coupled simulations. However, the stress distribution in the plies and in the bonding show differences. In the less sophisticated modeling approach with an overrated bonding thickness the stress peaks are smaller and distributed over a larger area. Due to the higher mass, the lowest eigenfrequency is decreased from 64 to 60 Hz. The resulting forces from the harmonic pitching motion are neglectable for the investigated case with a pitching frequency $f = 8$ Hz and an amplitude $\alpha_{\pm} = 8°$.

The CFD simulations for $Ma = 0.4$ and $Re = 1.2 - 1.6 \cdot 10^6$ reveal that the wind tunnel sidewall interference to the tip (distance = 250 mm) is small. A modified twist distribution leads to three regions of separated flow on the blade tip. The inboard dynamic stall is not triggered by the wind tunnel wall separation. Rotating viscous sidewalls do not change the flowfield significantly compared to simulations with non-rotating walls and grid deformation. The global lift peak difference of both simulation configurations is less than 1%. Therefore, the fast converging configuration with the rotating grid is proposed to generate load cases and study flow phenomena.

Fluid-structure interaction simulations for a steady state load case at $Ma = 0.4$, $Re = 1.2 \cdot 10^6$, and $\alpha = 10°$ revealed a less significant higher negative twist for $2.5°$ forward orientated spar caps and a corresponding lower lift coefficient of $\Delta C_L = 0.03$. Due to the negative twist, CFD loads calculated by means of a rigid simulation are conservative.

7 ACKNOWLEDGEMENTS

This work is funded by the DLR programmatic research in the project “STELAR”. The author would like to thank Mr. S. Sedlmair, Mr. J. Dillinger and Mrs. D. Dimitrov for the paper correction.

References

[1] McCroskey, W., “The phenomenon of dynamic stall.” Tech. rep., DTIC Document, 1981.

[2] Liiva, J., “Unsteady aerodynamic and stall effects on helicopter rotor blade airfoil sections.” *Journal of Aircraft*, Vol. 6, No. 1, 1969, pp. 46–51.

[3] Gardner, A., Richter, K., Mai, H., Altmikus, A., Klein, A., and Rohardt, C.-H., “Experimental investigation of dynamic stall performance for the EDI-M109 and EDI-M112 airfoils,” *Journal of the American Helicopter Society*, Vol. 58, No. 1, 2013, pp. 1–13.

[4] Le Pape, A., Pailhas, G., David, F., and Deluc, J., “Extensive wind tunnel tests measurements of dynamic stall phenomenon for the OA209 airfoil including 3D effects,” *Proceedings of the 33rd European Rotorcraft Forum*, 2007, pp. 320–335.

[5] Kaufmann, K., Costes, M., Richez, F., Gardner, A., and LePape, A., “Numerical investigation of three-dimensional dynamic stall on an oscillating finite wing,” *AHS 70th International Forum*, 2014.

[6] McCroskey, W. J., *Measurements of boundary layer transition, separation and streamline direction on rotating blades*, National Aeronautics and Space Administration, 1971.

[7] Mulleners, K., Kindler, K., and Raffel, M., “Dynamic stall on a fully equipped helicopter model,” *Aerospace Science and Technology*, Vol. 19, No. 1, 2012, pp. 72–76.

[8] Scott, M., Sigl, D., and Strawn, R., “Computational and Experimental Evaluation of Helicopter Rotor Tips for High Speed Forward Flight,” *AIAA paper*, Vol. 89, 1989, pp. 12–16.

[9] Mullins, B., Smith, D., Rath, C., and Thomas, S., “Helicopter Rotor Tip Shapes for Reduced Blade Vortex Interaction-An Experimental Investigation Part II,” *34th Aerospace Sciences Meeting and Exhibits, AIAA Paper*, No. 96-0149.

[10] Yeager, W. T., Jr., Noonan, K. W., Singleton, J. D., Wilbur, M. L., and Mirick, P. H., “Performance and Vibratory Loads Data From a Wind-Tunnel Test of a Model Helicopter MainRotor Blade With a Paddle-Type Tip,” Tech. rep., 1997.

[11] Brocklehurst, A. and Barakos, G., “A review of helicopter rotor blade tip shapes,” *Progress in Aerospace Sciences*, Vol. 56, 2013, pp. 35–74.

[12] Schimke, D., Link, S., and Schneider, S., “Noise and performance improved rotor blade for a helicopter,” *Patent EP 2 505 500 A1*, 03 2011.

[13] Wiggen, S. and Voss, G., “Development of a wind tunnel experiment for vortex dominated flow at a pitching Lambda wing,” *CEAS Aeronautical Journal*, 2014, pp. 1–10.

[14] Schewe, G., “Force and moment measurements in aerodynamics and aeroelasticity using piezoelectric transducers,” *Handbook of Experimental Fluid Mechanics*, 2007.

[15] Rauch, P., Gervais, M., P.Cranga, Baud, A., Hirsch, J.-F., Walter, A., and Beaumier, P., “Blue Edge: The

Design, Development and Testing of a New Blade Concept," *AHS 67th International Forum*, AHS, May 2011.

[16] Bailie, J., Ley, R., and Pasricha, A., "A summary and review of composite laminate design guidelines," *Langley RC, Hampton*, 1997.

[17] *ANSYS Mechanical APDL Theory Reference*, ANSYS, 2012.

[18] Neumann, J. and Krüger, W., "Coupling Strategies for Large Industrial Models," *Computational Flight Testing*, edited by N. Kroll, R. Radespiel, J. van der Burg, and K. Sorensen, Vol. 123 of *Notes on Numerical Fluid Mechanics and Multidisciplinary Design*, Springer, 2013, pp. 207–222.

[19] Hashin, Z., "Failure criteria for unidirectional fiber composites," *Journal of applied mechanics*, Vol. 47, No. 2, 1980, pp. 329–334.

[20] Gerhold, T., Friedrich, O., Evans, J., and Galle, M., "Calculation of complex three-dimensional configurations employing the DLR-TAU-code," *AIAA paper*, Vol. 167, 1997, pp. 1997.

[21] Menter, F. R., "Zonal two equation k-turbulence models for aerodynamic flows," *AIAA paper*, Vol. 2906, 1993, pp. 1993.

[22] Gardner, A., Richter, K., and Rosemann, H., "Prediction of the wind tunnel sidewall effect for the iGREEN wing-tailplane interference experiment," *New Results in Numerical and Experimental Fluid Mechanics VII*, Springer, 2010, pp. 75–82.

[23] Gerhold, T. and Neumann, J., "The parallel mesh deformation of the DLR TAU-code," *New results in numerical and experimental fluid mechanics VI*, Springer, 2008, pp. 162–169.

[24] Neumann, J. and Mai, H., "Gust Response: Simulation of an aeroelastic experiment by a fluid-structure interaction method," *Journal of Fluids and Structures*, Vol. 38, pp. 290–302.

8 COPYRIGHT STATEMENT